PHOTONICS Research

Mode crossing induced soliton frequency comb generation in high-*Q* yttria-stabilized zirconia crystalline optical microresonators

Guoping Lin[1,2,*] ⬛ and Tang Sun[1]

[1]*Ministry of Industry and Information Technology Key Laboratory of Micro-Nano Optoelectronic Information System, School of Science, Harbin Institute of Technology, Shenzhen 518055, China*
[2]*Innovation Center of Extreme Optics, Shanxi University, Taiyuan 030006, China*
Corresponding author: guoping.lin@hit.edu.cn

We demonstrate for the first time, to the best of our knowledge, the fabrication of high-*Q* crystalline optical microresonators from cubic yttria-stabilized zirconia (YSZ). Intrinsic *Q* factors up to 80 million are obtained, indicating an upper bound absorption coefficient of $0.001 \ cm^{-1}$ for YSZ crystals at the telecom wavelength. Through laser-scanned spectroscopy on a few-mode YSZ microresonator with a radius of 300 μm, we find that the mode crossing effect in the case of weak coupling can induce a repelling disruption of free spectral range values between transverse mode families. Generation of soliton and soliton crystals in such a YSZ microcomb platform operated in the normal dispersion regime is observed. A breathing comb behavior is also reported. Our finding has enriched comb generation platforms with potential multidisciplinary capabilities linked to properties of YSZ crystals in superconducting films and sensors.   © 2022 Chinese Laser Press

https://doi.org/10.1364/PRJ.441328

1. INTRODUCTION

Optical whispering gallery mode (WGM) microresonator platforms featuring both high quality (*Q*) factors and small mode volumes can greatly enhance light–matter interaction and have attracted great attention in the field of nonlinear photonics [1–5]. In particular, the generation of optical frequency combs based on Kerr nonlinearity has sparked intense focus in both fundamental researches and technical applications in recent years [6–8]. Such Kerr microcombs rely on the balance between the cavity and nonlinear dispersion. The onset of Kerr combs is also determined by the cavity loss and nonlinear gain. These parameters are related to properties of the cavity, the pump power, and the frequency detuning between the pump laser and cavity resonance. Through monitoring the transmission spectrum of a Kerr comb device, versatile comb behaviors including modulation instability (MI), chaos, and solitons have been discovered [6,7,9–13]. Among them, the phase-locked soliton comb to a short pulse in the time domain is of particular interest. Technical achievements using such combs have also been demonstrated in areas such as high-capacity optical data transfer and processing, laser ranging, and spectroscopy [7,14].

Cavity soliton combs typically coincide with an abrupt reduced power step. Due to thermal effects, such regimes usually

require specific approaches to access [7,14]. Recently, cavity solitons forming a crystal-like structure, referred to as soliton crystals, were found [10,15–20]. Avoided mode crossing (AMX) induced modulation on an intracavity continuous-wave (CW) background is found to cause the ordering of multiple Kerr solitons [10]. These soliton crystal states appear with larger conversion efficiencies and are much easier to access compared to regular soliton states. Manual tuning of the pump frequency is enough to locate a self-thermally locked position into the soliton crystal step. AMX aided Kerr frequency comb generation in the normal dispersion regime has been reported in silicon nitride (Si_3N_4) microresonators [21,22]. Breathing soliton crystals with a near-octave-spanning spectral range from an aluminum nitride (AlN) microring pumped in the anomalous dispersion regime have also been demonstrated [19]. Recently, applications in the radio frequency (RF) wave field based on soliton crystal microcombs have been explored [23,24].

On the other hand, Kerr frequency comb generation also benefits from its host material platforms [25]. The property of a high refractive index leads to a better light confinement ability. Various high index materials have been exploited for Kerr comb generation. Moreover, host materials with other nonlinearities can also enrich comb performances through multi-nonlinearity [26]. For instance, Kerr and Pockel nonlinearities in a lithium niobate ($LiNbO_3$) microring

resonator have been combined to produce a stable bi-chromatic soliton comb [27]. Considering oxide material platforms, yttria-stabilized zirconia (YSZ) has a high refractive index of 2.1 at the telecommunication wavelength. Its Kerr nonlinear coefficient is about 4×10^{-19}, similar to that of the popular Si_3N_4 platform [28]. YSZ also features good mechanical and chemical stabilities, which favors its potential applications in bendable or fordable devices [29] and integrated photonics [30].

In this work, for the first time to our knowledge, we report the fabrication of YSZ optical microresonators with high-Q factors up to 80 million at 1550 nm. A new absorption coefficient upper bound of about 0.001 cm^{-1} is obtained in this spectral window. We find that the mode coupling in a regular mode crossing is enough to cause local dispersion variation for creating soliton crystals. The pinning effect of the first comb sideband also assists in the generation of soliton crystals with multiple FSR spacing in a few-mode YSZ microresonator in the normal dispersion regime. Abrupt transmission steps are also found to be coincident with the generation of soliton crystals. A breathing comb behavior is observed. Our work shows that YSZ is a potential microplatform material for the application of Kerr microcombs. New applications could also arise considering its feature of good buffer layers for high-temperature superconducting films [31] and as host materials for rare-earth ions [32].

2. EXPERIMENTAL METHODS

A. Fabrication of YSZ Microcavities

High-Q YSZ disk microcavities were fabricated using the mechanical polishing method [33–36]. In the first step, a disk preform was cut from a commercial high-purity YSZ substrate as illustrated in Fig. 1(a). The preform was then carefully centered and attached to an aluminum post, which was later mounted on a spinning motor for further grinding and polishing with diamond slurries on the periphery of the disk rim. Figure 1(b) presents photos of a YSZ microdisk (cavity A) with a major radius of ~300 μm measured from both top and side views. The side view photo shows the microdisk sitting on the shaped mounting tip of the 6 mm diameter cylindrical post. The magnified image on the rim of the cavity gives a minor radius of ~118 μm with two wedge cuts to control and reduce modes as shown in Fig. 1(c). Successive total internal reflections then confine light in the rim of the disk and give rise to high-Q WGMs. It should be mentioned that a further polishing with sub-micrometer diamond slurries can be used to finely shift the resonances of the microcavity.

Also shown is the field distribution of several transverse mode families of WGMs. Besides the polarization of transverse electric (TE) and transverse magnetic (TM) modes, WGMs are characterized by three mode orders determining their field distributions. The azimuthal order m is related to longitudinal direction where the mode spacing of adjacent azimuthal modes is referred to as FSR of the cavity. The radial order q gives the number of field maxima in the radial direction, while the polar order $p + 1$ describes the number of field maxima in the polar direction as shown in Fig. 1(c). The polar order can be identified using the excitation mapping method [37]. The dispersion profile related to FSR values is mainly determined by the material dispersion and cavity geometry dispersion.
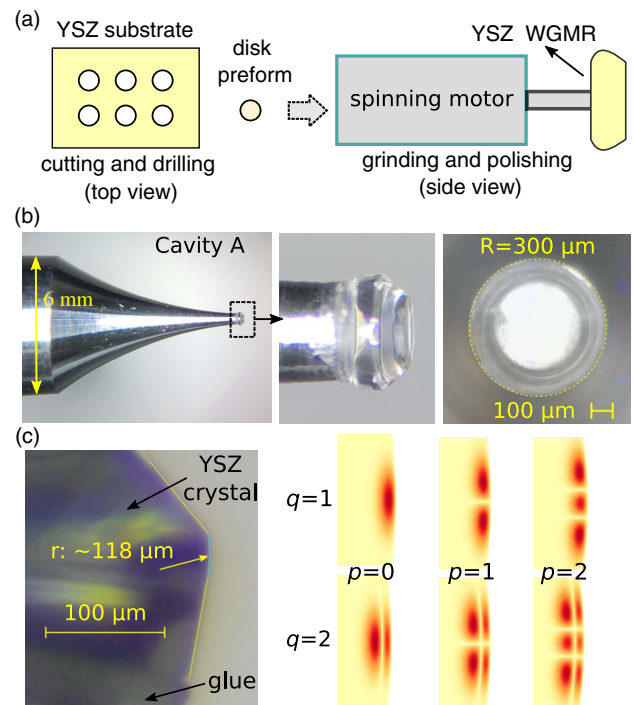

Fig. 1. (a) Illustrated fabrication method of YSZ microdisk resonator. (b) Left to right: side view photo of a YSZ microresonator mounted on an aluminum post; zoomed-in photo and top view of the microdisk showing a measured major radius R of about 300 μm. (c) Left: side view photo of the rim of the disk showing a minor radius r of about 118 μm. Right: field distributions of different transverse modes with radial and polar mode orders q and p of 1, 2 and 0, 1, 2, respectively.

The latter is affected by the dimension of the cavity geometry, which is usually fixed after fabrication, and by the transverse orders of the pump mode [38,39]. Although the polar mode order p weakly affects the total dispersion compared to the radial mode order, they both decide where the mode crossing may occur.

B. Experimental Setup

As the YSZ crystal features a refractive index of 2.11 at the telecom wavelength of 1550 nm, the rutile (TiO_2) optical prism with a higher refractive index is used for coupling light into the microresonator. The experimental setup illustrated in Fig. 2(a) is described as follows. A CW single frequency tunable laser around 1550 nm (Toptica CTL1500) was chosen as the light source for both laser-scanned spectroscopy and pumping. A fraction of the unable laser source was sent through a fiber ring etalon as a frequency reference [40]. The etalon consisted of a 2×2 (~1/99) fiber coupler and a 2 m long single mode fiber. Two 1% fiber ports are connected with the single mode fiber into a loop. The FSR value of the etalon FSR$_e$ was measured to be 48 MHz using RF sideband spectroscopy with a fiber electro-optic phase modulator (EOM) [41,42]. The pump laser power was boosted by an erbium doped fiber amplifier (EDFA) to about 170 mW for Kerr comb excitation. A fiber optical circulator (FOC) collected the feedback signals from the cavity for monitoring reflected mode signals through the
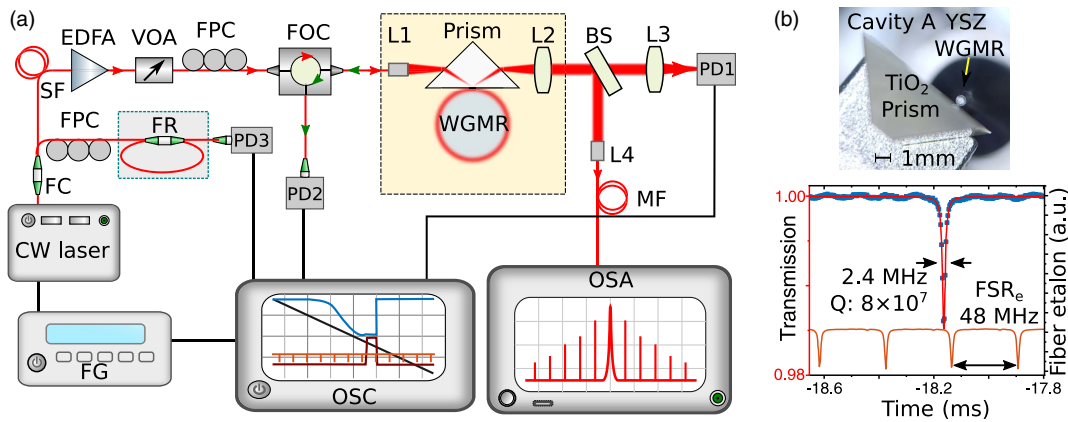
Fig. 2. (a) Schematic of the experimental setup. FC, fiber coupler; SF, single mode fiber; EDFA, erbium doped fiber amplifier; VOA, variable optical attenuator; FPC, fiber polarization controller; FR: fiber ring etalon; FOC, fiber optical circulator; L, optical lens; PD, photodetector; MF, multimode fiber; FG, function generator; OSC, digital oscilloscope; OSA, optical spectrum analyzer. (b) Top: photo of the YSZ microresonator and TiO$_2$ prism coupler. Bottom: laser-scanned transmission spectrum of a WGM in the YSZ microresonator showing a linewidth of 2.4 MHz indicating a Q factor of 8×10^7. FSR$_e$: FSR value of the fiber ring etalon.

Rayleigh effect. The transmitted signal through the prism coupled resonator was collected and split into two parts: one was focused onto the photodetector (PD1), and the other was coupled into a multimode fiber connected to an optical spectrum analyzer (OSA, Yokogawa 6370D) for characterizing the comb spectrum. Although the multimode fiber input decreases the spectral resolution, the coupling of light from free space is much easier to align. Since leg surfaces of the right angle prism are uncoated, p-polarized incident beams are expected to experience lower Fresnel reflection losses in the case of an optimized incident coupling angle for a YSZ microresonator. We thereby chose to excite TM WGMs in the resonator during the experiment.

3. RESULTS AND DISCUSSION

A. Q Factors at the Telecommunication Wavelength

The evanescent coupling gap between the microresonator and the prism was controlled through a piezo-actuator. The photo of the coupled resonator is shown in Fig. 2(b) (top). Also presented in this figure is the laser-scanned transmission spectrum across an under-coupled WGM of the YSZ microresonator. A Lorentzian fit of the resonance peak gives a linewidth of 2.4 MHz around 1550 nm, indicating an intrinsic Q factor of 8×10^7. It should be noted that the intrinsic Q of a cavity is determined by $1/Q = 1/Q_{ss} + 1/Q_\alpha + 1/Q_r$ with subscripts ss, α, and r describing scattering, absorption, and radiation related losses, respectively [41]. Thereby, the measured Q can give an upper bound of the material absorption coefficient considering that $Q_\alpha = 2\pi n_0/(\lambda\alpha)$. As a result, we derive a material absorption upper bound of about 0.001 cm^{-1} for YSZ. We also fabricated millimeter-size YSZ disks and confirmed the Q factor measurements.

However, it was found that the intrinsic Q factor degraded during repeated resonator cleaning, dispersion, and comb measurements. We placed another high-Q YSZ resonator in the setup to monitor the Q factor of 7.4×10^7 for a selected mode over 24 h. It was found that the Q factor did not degrade. Thereby, we infer that the Q factor in this level is not sensitive

to humidity. Moreover, we repeatedly cleaned the degraded resonator, but the intrinsic Q factor remained unchanged. We suspect that the degraded Q factor could result from surface degradation due to mis-positioning of the prism coupler or failed attempts to further increase the Q factor with nanodiamond slurries.

B. Mode Crossing

It has been shown that the generation of soliton crystal combs is linked to mode crossing phenomena in microcavities [10]. Here, we carried out laser-scanned spectroscopy on cavity A featuring a few modes within one FSR to reveal mode crossing effects. Figure 3(a) shows the spectroscopy result over a 17 nm spectral window. The bottom curve is the simultaneously recorded fiber etalon signals as frequency markers. It is found that the free spectral range of the cavity around 1550 nm is about 0.6 nm through both optical spectrum and transmission spectrum analysis. One clearly sees that only two mode families feature the best mode contrast over 20% within one FSR. Zoomed-in spectra as shown in the inset of Fig. 3(a) give two examples of the mode spacing between these two transverse modes (A and B). We plot the absolute values of mode spacing between modes A and B families as a function of the center wavelengths between them in Fig. 3(b). The mode crossing phenomenon is clearly visible around 1553.4 nm where the mode spacing reaches its minimum. Examples of Kerr frequency comb spectra when pumping mode A families are presented as insets. We observe the pinning phenomenon of the first comb line around the crossing regime. Abrupt transmission steps appear to be coincident with the comb generation, in agreement with reported soliton crystal generation [15]. For the pump mode in the mode crossing regime where the spacing between modes A and B reaches the minimum, we find the generation of a symmetric Kerr comb.

Through observing the spacing distribution of each mode family in Fig. 3, it is still difficult to determine the mode coupling conditions. We thereby further derive the FSR values of modes A and B families. For clarity, we first plot relative
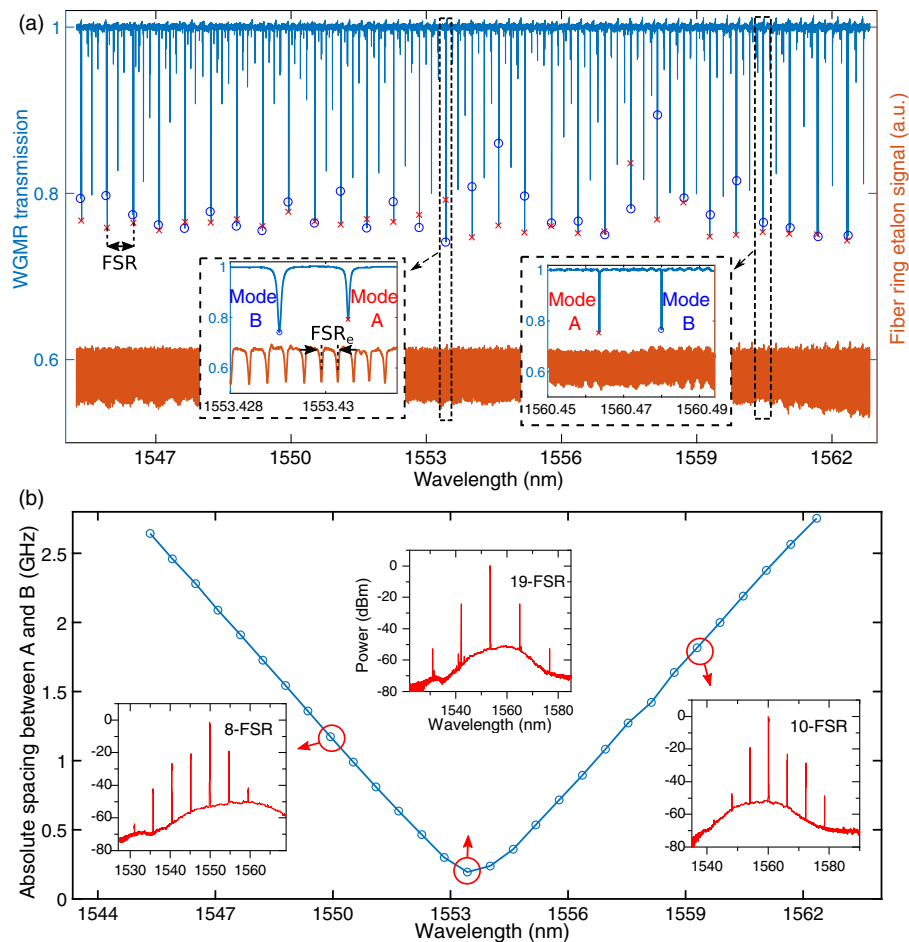
Fig. 3. Mode crossing in the YSZ microresonator. (a) Laser-scanned transmission spectrum covering a 30-FSR spectral range of the YSZ micro-resonator (cavity A) with fiber etalon signals simultaneously captured for wavelength or frequency range calibration. Red crosses: mode A family. Blue circles: mode B family. FSR, FSR of WGMs; FSR_e: FSR of the fiber ring etalon. (b) Absolute mode spacing between modes A and B as a function of the centered wavelength between them. Examples of Kerr frequency comb spectra pumped at mode A are shown in the insets.

frequency positions of both modes A and B families in Fig. 4(a). A constant increment of one FSR value $D_1/2\pi$ of 74.5 GHz is used for both subtractions in each plot, such that the mode crossing effect can be clearly seen. Here, weak coupling of modes instead of AMX is observed. The mode coupling occurs in a single resonator when two longitudinal mode families overlap in space. As their resonant center frequencies approach each other, the resulting mode interaction leads to a frequency shift and thereby changes the local dispersion. Both regular mode crossing and AMX have been reported in other microcomb platforms [21,43]. By plotting FSR values of modes A and B families as a function of resonant wavelengths as shown in Fig. 4(b), we find that the mode coupling has induced a repelling effect on FSR variations of both modes, where FSR shifts away from each family. In contrast, it has been previously reported that AMX can lead to an appealing effect on FSR values between two mode families [21]. The disruption of FSR values can thereby lead to local variations of dispersion conditions and assist in the generation of Kerr frequency combs.

To theoretically investigate the total dispersion profile of this cavity, we calculated the eigenfrequencies by using the analytical approximation of WGMs in a toroid [44,45]. We use a major radius of 300.24 μm and a minor radius of 118.18 μm for the calculation. The Sellmeier equation of YSZ is utilized to take into account the material dispersion. By solving the formulation, we find that the estimated eigen-frequencies of $q = 1, p = 0$ and $q = 2, p = 2$ modes are coincident with modes A and B families as shown in both Figs. 4(a) and 4(b) as solid lines. Although such analytical estimates of WGM positions still lack precision compared to numerical results using the finite element method—often used in Kerr microcomb designs [7]—the analytical solution does provide quick insight into tailoring WGM dispersion [38].

In general, anomalous dispersion refers to decreased FSR values as wavelengths increase and vice versa [39]. When second order dispersion $D_2/2\pi$ is dominant, this parameter then equals the difference between adjacent FSR values ΔFSR. In the case of a fiber ring etalon, we can theoretically derive a $D_{2e}/2\pi$ of about 49.1 mHz at 1550 nm. Considering the FSR of the whispering gallery mode resonator (WGMR) of 74.5 GHz and the etalon FSR_e, the dispersion of the fiber eta-lon contributes ~60 kHz deviation from the equidistant grid of
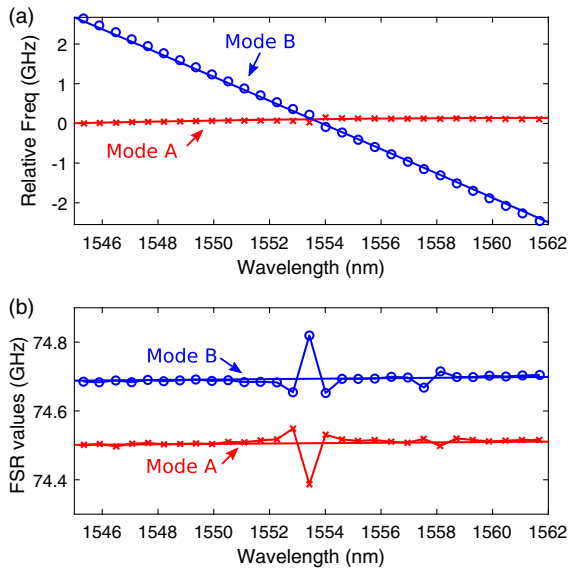
Fig. 4. Mode coupling in the YSZ microcavity. (a) Relative frequency position of modes A and B families showing a crossing position near 1554 nm. (b) FSR values of modes A and B families with the observed weak mode coupling induced disturbance. Solid lines: calculated analytical estimated data.

the etalon FSR. For an adjacent FSR of the whispering gallery mode resonator (WGMR), the difference of such deviation is of the order of ~1 kHz, which is much smaller than the large normal dispersion with $D_2/2\pi$ of $\sim$ –340 kHz for the fundamental WGM family of the YSZ microresonator. To minimize the jitter of etalon signals, we took average values from 10 FSR_e values around the WGM peaks of interest and neglected the dispersion of the etalon. It should be noted that the dispersion of the etalon should be taken into account for other resonators with similar orders of dispersion.

1. Generation of Soliton and Crystals in the Few-Mode Cavity

YSZ cavity A was fabricated such that only the sharp rim of the disk was selectively fine polished. As a result, many high-order transverse WGMs encounter higher scattering losses when their mode fields reach the rough surface. Furthermore, the prism coupling setup can be used to excite mainly low-order modes with an optimized incident angle of the input beam. Therefore, we were able to observe the few-mode spectrum in such a cavity as shown in Fig. 3. We refer to this cavity as the few-mode cavity.

The generation of Kerr frequency combs relies strongly on many parameters including pump power, detuning frequency of the pump laser from the mode, and the dispersion profile. Versatile comb regimes can be excited depending on parameters such as an MI comb, chaotic comb, breathing solitons, single solitons, and soliton crystals [10]. The pump power should not be too much above threshold for accessing phase-locked solitons. The threshold of a Kerr frequency comb can be estimated by [46]

$$P_{\text{th}} \approx 1.54 \frac{\pi}{2} \frac{1}{\eta} \frac{n}{n_2} \frac{\omega}{D_1} \frac{A}{Q_L^2}, \tag{1}$$

where η is the coupling factor, n is the refractive index of the cavity, n_2 is the effective Kerr coefficient, $\omega/2\pi$ is the resonant frequency, $D_1/2\pi$ is the FSR value, A is the mode area, and Q_L is the loaded Q factor. Considering the case of the YSZ microcavity in this experiment, the estimated mode area A for $q = 1$, $p = 0$, and $m = 2542$ is about 18 μm^2 using the analytical approximation in Ref. [44].

We then use n_2 of 4×10^{-19} $m^2 \cdot W^{-1}$ [28], FSR of 74.5 GHz, n of 2.1, and η of 1 for the in-coupled threshold. The estimated in-coupled threshold is about 1.5 mW. In our experiment, we have observed the onset of Kerr combs at the threshold of absorbed pump power of about 2.1 mW. If we take into account the expected Fresnel reflection loss of 11%, this value would be about 1.9 mW. To generate soliton crystal combs, we use an incident pump power around 170 mW at the prism. The maximum coupling contrast of WGMs is about 20% in our setup. For Kerr comb generation, the under-coupled condition is used. Therefore, the actual in-coupled pump power is usually less than 30 mW.

Due to the presence of Rayleigh scattering in the high-Q resonator, we are able to monitor the comb line power in the backward direction of the signal. Note that the comb signal can be easily distinguished from the reflected coupled pump power since soliton or soliton crystal microcombs occur with the concurrent appearance of an abrupt transmission step or an increased comb power step [10]. Such steps are also coincident with the phase-locking transition steps in either pure Kerr combs or Raman–Kerr combs [47]. Unlike integrated comb platforms, the coupling gap in our experiment can be conveniently altered through a piezo controller. Therefore, it is possible to find a specific coupling gap under which condition the soliton step becomes very unstable and can quickly switch its appearance (see Visualization 1).

Figure 5 shows the observation of a single soliton frequency comb transition in YSZ cavity A when pumping mode A at 1554.7 nm. The coupling condition was under-coupled. The appearance of the soliton step in the transmission spectrum is highlighted with a green background in Fig. 5(a). We find that this step accompanies the observation of Kerr combs in the normal dispersion regime, similar to that of the reported mode crossing induced soliton crystals [15]. The self-thermal locking regime can be easily accessed when pump mode A is on the blue side of mode B. In this experiment, we stopped laser scanning and manually located the thermal locking of the pump frequency into mode A. We observed a comb spectrum clearly disrupted by the mode crossing as shown in Fig. 5(b) (left). The first comb line appears to be pinned at the mode around 1554.1 nm, while the comb line power encountered a sudden drop at the mode around 1553.5 nm. It is consistent with the reported pinning effect and the envelope disruption of the mode crossing in the Kerr comb spectrum [21,43]. However, when we further redshifted the wavelength of the pump laser in regime II, a stable single FSR spaced soliton comb was then formed as shown in Fig. 5(b) (right). The envelope of the comb fits well with a sech^2 shape. It should be emphasized that the generation of such a single soliton comb is repeatedly manually accessed due to the pinning effect of the first sideband. Moreover, the appearance of the transmission step is
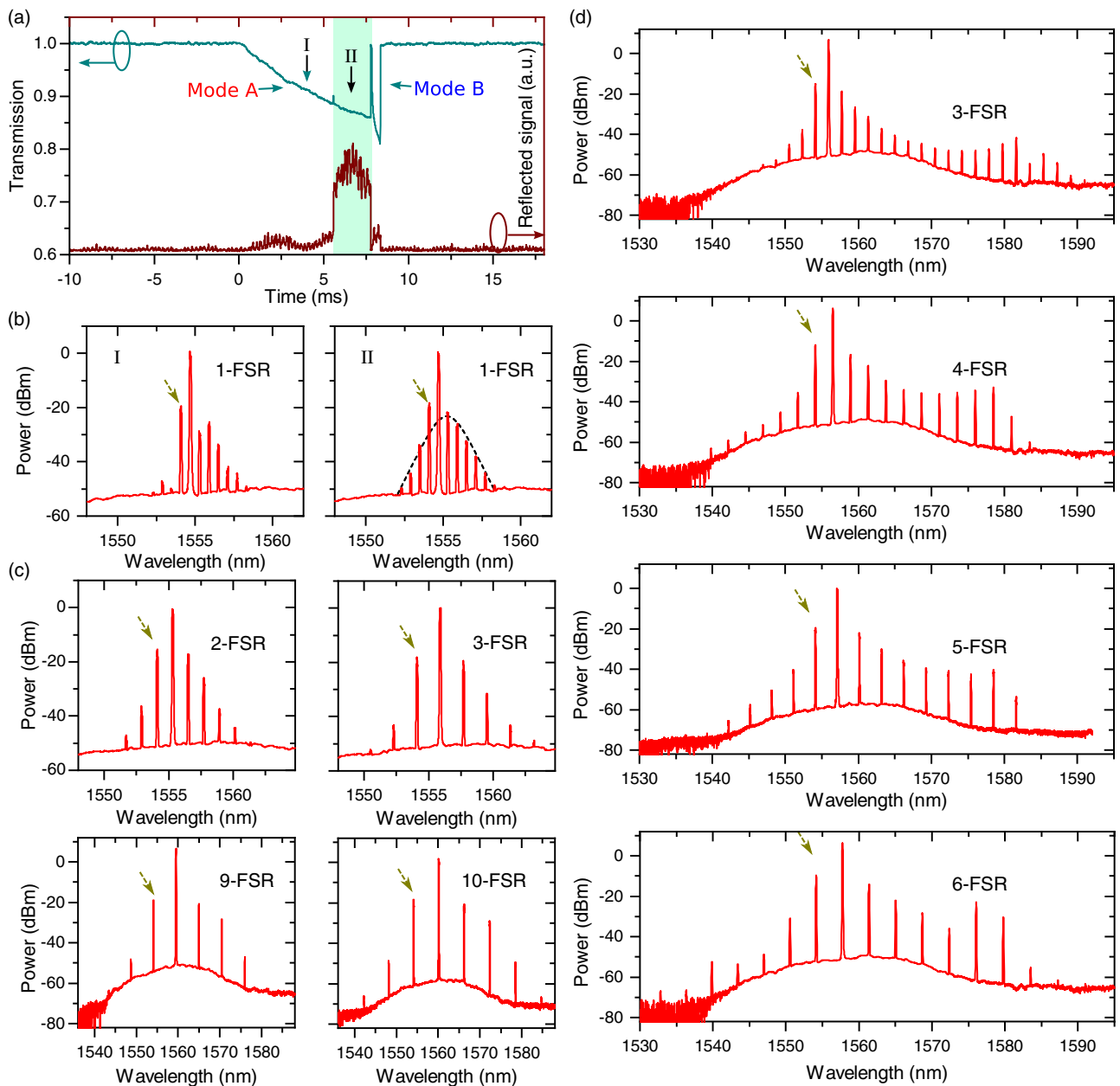
Fig. 5. Soliton and soliton crystal frequency comb generation pumped at mode A family. (a) Pump scanned transmission spectrum around 1554.7 nm over about 6 GHz spectral range showing a soliton step coincident with the increased feedback power regime. (b) Comb spectra obtained with the pump thermally locked to mode A. Dashed line: $sech^2$ envelope fit. (c) Optical spectra of soliton crystal with four different soliton numbers, where pump modes belong to mode A family. Pump wavelengths are 1555.3 nm, 1555.9 nm, 1559.5 nm, and 1560.1 nm from left to right and top to bottom. (d) Comb spectra showing a dispersive-wave-like tail around 1580 nm. Pump wavelengths are 1555.9 nm, 1556.5 nm, 1557.1 nm, and 1557.7 nm from top to bottom. Note that the brown arrow marks the pinned peak at 1554.1 nm.

similar to those of soliton crystals [10]. It is therefore easy to access and is more efficient than traditional single Kerr solitons.

We further chose to pump other adjacent mode A families and observed similar transmission steps in the forward direction, while an abrupt increased signal power step appeared in the backward direction. Using self-thermal locking [48], we obtained the generation of soliton crystal combs with different comb line spacings. Figure 5(c) shows examples of such spectra with 2-FSR, 3-FSR, 9-FSR, and 10-FSR spacings when the pump modes are around 1555.3 nm, 1555.9 nm, 1559.5 nm, and 1560.1 nm, respectively. It is found that the pinned first comb lines all appear around 1554.1 nm. The power of this comb line is found to be stronger than others. In particular, we observed wider comb spectra with line spacing from 3-FSR to 6-FSR with dispersive-wave-like tails as shown in Fig. 5(d), which could result from the dispersive wave induced by other mode interactions [43].

Furthermore, we studied the evolution of the soliton crystal combs in such a cavity as shown in Fig. 6. The pump laser frequency was first scanned across mode A around 1555.8 nm, and the coupling gap was optimized for comb generation. We then stopped the laser ramping, manually tuned the laser wavelength into the resonance, and recorded the corresponding comb spectra. Figures 6(a)–6(c) present comb spectra in three different detuning regimes marked in the transmission spectrum in the inset of Fig. 6(d). As the wavelength was redshifted and self-thermally locked to the resonance, the primary comb with 3-FSR spacing, the breathing comb with 1-FSR spacing, and the soliton crystal comb with 3-FSR spacing were observed, respectively. We used the fast Fourier transform (FFT) function of the oscilloscope (R & S RTB2004, bandwidth 200 MHz) to obtain the corresponding RF power spectrum from PD1 (Thorlabs PDA05CF2, bandwidth 150 MHz). Visible breathing behavior at the frequency of about 7.3 MHz was found in detuning regime ii, which is consistent with the oscillatory trace in the time domain as shown in the inset of Fig. 6(e). Our observation is similar to those breathing combs in either anomalous or normal dispersion cavities [11,19,49]. In particular, we find that regime ii can be fully suppressed by optimizing the coupling gap. It should be mentioned that the breathing behavior was also observed before visible 1-FSR comb lines were filled in.

2. Kerr Combs in an Over-Mode Microresonator

In addition, we also investigate the comb generation with another YSZ microresonator (cavity B) with a major radius of about 456 μm. This resonator supports rich transverse high-Q modes within one FSR and is referred to as an over-mode microresonator [50]. In comparison with the engineered few-mode cavity A, mode crossing phenomena are apparently more common. As a result, we find that abrupt steps together with

the comb generation became much easier to find. Within one FSR spectral range, several mode families featuring abrupt transmission steps were found. Figure 7(a) shows an example of the transmission spectrum covering about a 12 GHz range. Two modes appear with the transmission steps as highlighted in green. These steps were verified by adjusting the coupling gap such that they became unstable and vanished time after time (see Visualization 2). The inset presents the photo of cavity B coupled with the rutile prism.
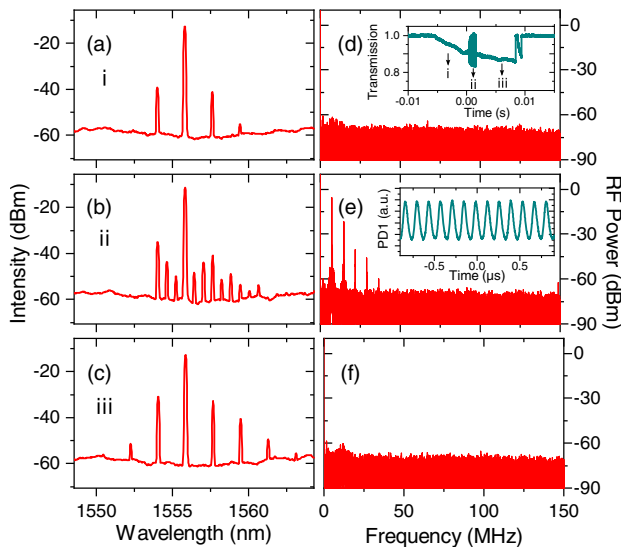

Fig. 7. Kerr optical frequency comb generation in a YSZ microresonator with a radius of about 456 μm (cavity B). (a) Transmission spectrum spanning a spectral window of 11.9 GHz showing two adjacent WGMs with soliton crystal steps. Inset: photo of the microcavity coupled with the rutile prism. The appearance of the transmission step of mode A is recorded (see Visualization 2). (b) Different optical comb spectra obtained when the pump laser is thermally locked to the soliton crystal step in mode A. (c) Soliton crystal comb obtained when the pump laser is thermally locked to the step of mode B.

Fig. 6. Evolution of soliton crystal comb generation during pump laser scanning. (a)–(c) Typical optical comb spectra. (d)–(f) Corresponding RF spectra obtained by FFT in the oscilloscope. Inset in (d): transmission spectrum in cavity A when the laser wavelength is scanned across mode A around 1555.8 nm. Inset in (e): corresponding temporal trace in the oscilloscope.
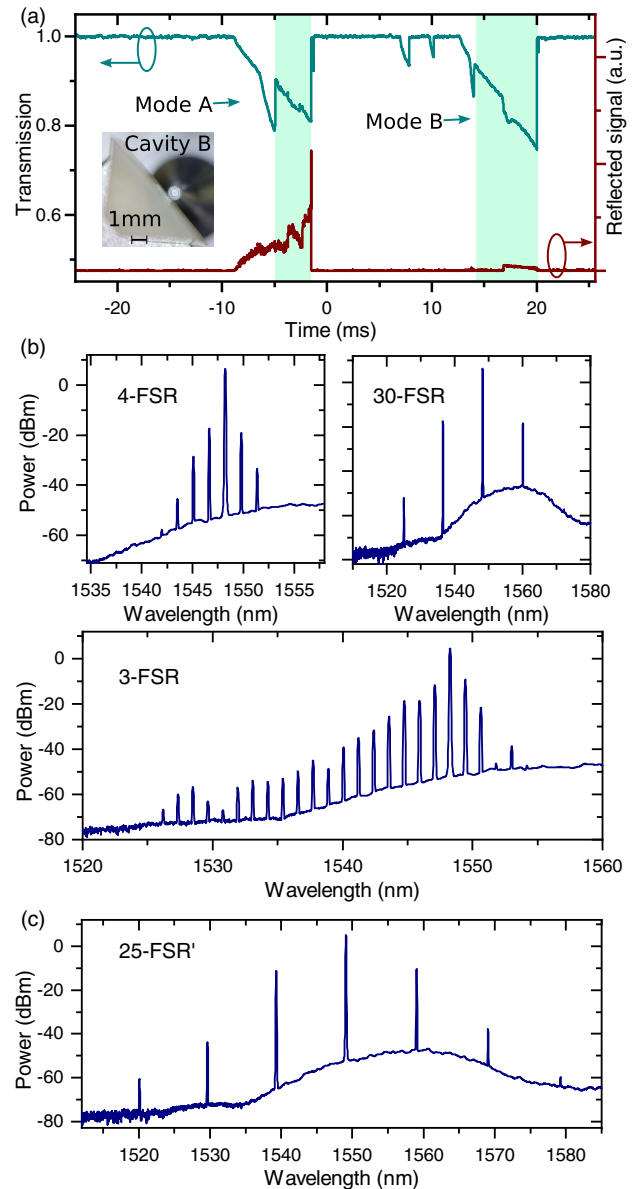
Table 1.   Performances of Various Kerr Microcombs on High Refractive Index ($n > 2$) Platforms

Material	Refractive Index	n_2 (m$^2 \cdot$W^{-1})	FSR (GHz)	Mode Area (μm^2)	Loaded Q	Lowest Threshold (mW)
Si$_3$N$_4$	2.0	2.5×10^{-19}	200	~1.5	~4×10^6	0.33 [51]
AlN	2.1	3.5×10^{-19}	364	–	~0.8×10^6	55 [52]
LiNbO$_3$	2.21	1.8×10^{-19}	200	~1	~2×10^6	4.2 [27]
Diamond	2.4	0.8×10^{-19}	925	~0.8	~1×10^6	20 [53]
4H silicon carbide	2.6	8×10^{-19}	260	~2.5	~4×10^6	10 [54]
Gallium phosphide	3.1	~1×10^{-17}	250	~0.15	~0.2×10^6	3 [55]
AlGaAs	3.3	2.6×10^{-17}	1000	~0.28	~1×10^6	0.036 [56]
Si (pumped at 2.6 μm)	3.5	1×10^{-18}	127	~2	~2.2×10^5	3 [57]
YSZ (this work)	2.1	~4×10^{-19}	74.5	~18	~2×10^7	1.9

When the pump laser was thermally locked to the transmission step of mode A in cavity B, we found that Kerr combs with very different frequency spacings could be generated depending on the detuning of the pump. For instance, the Kerr comb with 4-FSR or 0.2 THz frequency spacing transited into the comb with 30-FSR or 1.48 THz frequency spacing when the pump wavelength was redshifted. Further redshifting the pump wavelength, a very asymmetric comb with 3-FSR spacing was obtained as shown in Fig. 7(b). For pump mode B, we observed a relatively weaker feedback signal. However, it should be mentioned that the feedback strength of a Kerr comb in the cavity does not rely merely on comb power, since it is also determined by Rayleigh scattering strength. When pumping into this mode, we found less complicated comb transitions. A comb with 1.24 THz spacing or 25-FSR' was observed as shown in Fig. 7(c).

4. CONCLUSION

To the best of our knowledge, we have demonstrated the fabrication of the first high-Q YSZ WGM optical microresonators. We obtained a new upper bound absorption coefficient of YSZ at the telecom wavelength. We further report the generation of soliton crystal Kerr combs in a few-mode YSZ microresonator assisted by mode interactions. Table 1 presents the performances of reported low threshold Kerr microcomb platforms made from different optical materials with high refractive indices larger than 2.0. Although the comb spanning is quite limited due to the large normal dispersion, our work paves the way for further design of on-chip YSZ wideband microcombs in abnormal dispersion. New opportunities with high-Q YSZ optical microresonators could arise when considering its high chemical and thermal stability and mechanical flexibility, ideal for bendable devices for light sources and sensors.

REFERENCES

1. D. V. Strekalov, C. Marquardt, A. B. Matsko, H. G. Schwefel, and G. Leuchs, "Nonlinear and quantum optics with whispering gallery resonators," J. Opt. **18**, 123002 (2016).
2. I. Breunig, "Three-wave mixing in whispering gallery resonators," Laser Photon. Rev. **10**, 569–587 (2016).
3. L. Ge, L. Feng, and H. G. Schwefel, "Optical microcavities: new understandings and developments," Photon. Res. **5**, OM1–OM3 (2017).
4. G. Lin, A. Coillet, and Y. K. Chembo, "Nonlinear photonics with high-Q whispering-gallery-mode resonators," Adv. Opt. Photon. **9**, 828–890 (2017).
5. G. Lin and Y. K. Chembo, "Monolithic total internal reflection resonators for applications in photonics," Opt. Mater. X **2**, 100017 (2019).
6. A. Pasquazi, M. Peccianti, L. Razzari, D. J. Moss, S. Coen, M. Erkintalo, Y. K. Chembo, T. Hansson, S. Wabnitz, P. Del'Haye, X. Xue, A. M. Weiner, and R. Morandotti, "Micro-combs: a novel generation of optical sources," Phys. Rep. **729**, 1–81 (2018).
7. T. J. Kippenberg, A. L. Gaeta, M. Lipson, and M. L. Gorodetsky, "Dissipative Kerr solitons in optical microresonators," Science **361**, eaan8083 (2018).
8. A. L. Gaeta, M. Lipson, and T. J. Kippenberg, "Photonic-chip-based frequency combs," Nat. Photonics **13**, 158–169 (2019).
9. C. Godey, I. V. Balakireva, A. Coillet, and Y. K. Chembo, "Stability analysis of the spatiotemporal Lugiato-Lefever model for Kerr optical frequency combs in the anomalous and normal dispersion regimes," Phys. Rev. A **89**, 063814 (2014).
10. M. Karpov, M. H. Pfeiffer, H. Guo, W. Weng, J. Liu, and T. J. Kippenberg, "Dynamics of soliton crystals in optical microresonators," Nat. Phys. **15**, 1071–1077 (2019).
11. S. Wan, R. Niu, Z.-Y. Wang, J.-L. Peng, M. Li, J. Li, G.-C. Guo, C.-L. Zou, and C.-H. Dong, "Frequency stabilization and tuning of breathing solitons in Si$_3$N$_4$ microresonators," Photon. Res. **8**, 1342–1349 (2020).
12. H. Weng, J. Liu, A. A. Afridi, J. Li, J. Dai, X. Ma, Y. Zhang, Q. Lu, J. F. Donegan, and W. Guo, "Directly accessing octave-spanning dissipative Kerr soliton frequency combs in an AlN microresonator," Photon. Res. **9**, 1351–1357 (2021).
13. X. Wang, P. Xie, W. Wang, Y. Wang, Z. Lu, L. Wang, S. T. Chu, B. E. Little, W. Zhao, and W. Zhang, "Program-controlled single soliton microcomb source," Photon. Res. **9**, 66–72 (2021).
14. W. Wang, L. Wang, and W. Zhang, "Advances in soliton microcomb generation," Adv. Photon. **2**, 034001 (2020).
15. D. C. Cole, E. S. Lamb, P. Del'Haye, S. A. Diddams, and S. B. Papp, "Soliton crystals in Kerr resonators," Nat. Photonics **11**, 671–676 (2017).
16. W. Wang, Z. Lu, W. Zhang, S. T. Chu, B. E. Little, L. Wang, X. Xie, M. Liu, Q. Yang, L. Wang, J. Zhao, G. Wang, Q. Sun, Y. Liu, Y. Wang, and W. Zhao, "Robust soliton crystals in a thermally controlled microresonator," Opt. Lett. **43**, 2002–2005 (2018).
17. Y. He, J. Ling, M. Li, and Q. Lin, "Perfect soliton crystals on demand," Laser Photon. Rev. **14**, 1900339 (2020).
18. Z. Lu, H.-J. Chen, W. Wang, L. Yao, Y. Wang, Y. Yu, B. Little, S. Chu, Q. Gong, W. Zhao, X. Yi, Y.-F. Xiao, and W. Zhang, "Synthesized soliton crystals," Nat. Commun. **12**, 3179 (2021).

19. H. Weng, A. A. Afridi, J. Liu, J. Li, J. Dai, X. Ma, Y. Zhang, Q. Lu, W. Guo, and J. F. Donegan, "Near-octave-spanning breathing soliton crystal in an AlN microresonator," Opt. Lett. **46**, 3436–3439 (2021).

20. T. Huang, J. Pan, Z. Cheng, G. Xu, Z. Wu, T. Du, S. Zeng, and P. P. Shum, "Nonlinear-mode-coupling-induced soliton crystal dynamics in optical microresonators," Phys. Rev. A **103**, 023502 (2021).

21. Y. Liu, Y. Xuan, X. Xue, P.-H. Wang, S. Chen, A. J. Metcalf, J. Wang, D. E. Leaird, M. Qi, and A. M. Weiner, "Investigation of mode coupling in normal-dispersion silicon nitride microresonators for Kerr frequency comb generation," Optica **1**, 137–144 (2014).

22. X. Xue, Y. Xuan, P.-H. Wang, Y. Liu, D. E. Leaird, M. Qi, and A. M. Weiner, "Normal-dispersion microcombs enabled by controllable mode interactions," Laser Photon. Rev. **9**, L23–L28 (2015).

23. M. Tan, X. Xu, A. Boes, B. Corcoran, J. Wu, T. G. Nguyen, S. T. Chu, B. E. Little, R. Morandotti, A. Mitchell, and D. J. Moss, "Photonic RF arbitrary waveform generator based on a soliton crystal micro-comb source," J. Lightwave Technol. **38**, 6221–6226 (2020).

24. X. Xu, M. Tan, J. Wu, A. Boes, T. G. Nguyen, S. T. Chu, B. E. Little, R. Morandotti, A. Mitchell, and D. J. Moss, "Broadband photonic RF channelizer with 92 channels based on a soliton crystal microcomb," J. Lightwave Technol. **38**, 5116–5121 (2020).

25. A. Kovach, D. Chen, J. He, H. Choi, A. H. Dogan, M. Ghasemkhani, H. Taheri, and A. M. Armani, "Emerging material systems for integrated optical Kerr frequency combs," Adv. Opt. Photon. **12**, 135–222 (2020).

26. G. Lin and Q. Song, "Kerr frequency comb interaction with Raman, Brillouin, and second order nonlinear effects," Laser Photon. Rev. **16**, 2100184 (2022).

27. Y. He, Q.-F. Yang, J. Ling, R. Luo, H. Liang, M. Li, B. Shen, H. Wang, K. Vahala, and Q. Lin, "Self-starting bi-chromatic LiNBO$_3$ soliton microcomb," Optica **6**, 1138–1144 (2019).

28. G. Marcaud, S. Serna, K. Panaghiotis, C. Alonso-Ramos, X. L. Roux, M. Berciano, T. Maroutian, G. Agnus, P. Aubert, A. Jollivet, A. Ruiz-Caridad, L. Largeau, N. Isac, E. Cassan, S. Matzen, N. Dubreuil, M. Rérat, P. Lecoeur, and L. Vivien, "Third-order nonlinear optical susceptibility of crystalline oxide yttria-stabilized zirconia," Photon. Res. **8**, 110–120 (2020).

29. K. K. Gopalan, D. Rodrigo, B. Paulillo, K. K. Soni, and V. Pruneri, "Ultrathin yttria-stabilized zirconia as a flexible and stable substrate for infrared nano-optics," Adv. Opt. Mater. **7**, 1800966 (2019).

30. G. Marcaud, S. Matzen, C. Alonso-Ramos, X. Le Roux, M. Berciano, T. Maroutian, G. Agnus, P. Aubert, L. Largeau, V. Pillard, S. Serna, D. Benedikovic, C. Pendenque, E. Cassan, D. Marris-Morini, P. Lecoeur, and L. Vivien, "High-quality crystalline yttria-stabilized-zirconia thin layer for photonic applications," Phys. Rev. Mater. **2**, 035202 (2018).

31. X. D. Wu, S. R. Foltyn, P. N. Arendt, W. R. Blumenthal, I. H. Campbell, J. D. Cotton, J. Y. Coulter, W. L. Hults, M. P. Maley, H. F. Safar, and J. L. Smith, "Properties of YBa$_2$Cu$_3$O$_{7-\delta}$ thick films on flexible buffered metallic substrates," Appl. Phys. Lett. **67**, 2397–2399 (1995).

32. X. Hong, S. Xu, X. Wang, D. Wang, S. Li, B. A. Goodman, and W. Deng, "Growth, structure and optical spectroscopic properties of dysprosia-doped cubic yttria stabilized zirconia (YSZ) single crystals," J. Lumin. **231**, 117766 (2021).

33. W. Liang, A. A. Savchenkov, V. S. Ilchenko, D. Eliyahu, D. Seidel, A. B. Matsko, and L. Maleki, "Generation of a coherent near-infrared Kerr frequency comb in a monolithic microresonator with normal GVD," Opt. Lett. **39**, 2920–2923 (2014).

34. G. Lin, S. Diallo, R. Henriet, M. Jacquot, and Y. K. Chembo, "Barium fluoride whispering-gallery-mode disk-resonator with one billion quality-factor," Opt. Lett. **39**, 6009–6012 (2014).

35. S. Fujii, Y. Hayama, K. Imamura, H. Kumazaki, Y. Kakinuma, and T. Tanabe, "All-precision-machining fabrication of ultrahigh-Q crystalline optical microresonators," Optica **7**, 694–701 (2020).

36. A. Danilin, G. Slinkov, V. Lobanov, K. Min'kov, and I. Bilenko, "Magneto-optical effects in a high-Q whispering-gallery-mode resonator with a large Verdet constant," Opt. Lett. **46**, 2509–2512 (2021).

37. G. Lin, B. Qian, F. Oručević, Y. Candela, J.-B. Jager, Z. Cai, V. Lefèvre-Seguin, and J. Hare, "Excitation mapping of whispering gallery modes in silica microcavities," Opt. Lett. **35**, 583–585 (2010).

38. G. Lin and Y. K. Chembo, "On the dispersion management of fluorite whispering-gallery mode resonators for Kerr optical frequency comb generation in the telecom and mid-infrared range," Opt. Express **23**, 1594–1604 (2015).

39. S. Fujii and T. Tanabe, "Dispersion engineering and measurement of whispering gallery mode microresonator for Kerr frequency comb generation," Nanophotonics **9**, 1087–1104 (2020).

40. X. Zhang, G. Lin, T. Sun, Q. Song, G. Xiao, and H. Luo, "Dispersion engineering and measurement in crystalline microresonators using a fiber ring etalon," Photon. Res. **9**, 2222–2229 (2021).

41. G. Lin, J. Fürst, D. V. Strekalov, I. S. Grudinin, and N. Yu, "High-Q UV whispering gallery mode resonators made of angle-cut BBO crystals," Opt. Express **20**, 21372–21378 (2012).

42. J. Li, H. Lee, K. Y. Yang, and K. J. Vahala, "Sideband spectroscopy and dispersion measurement in microcavities," Opt. Express **20**, 26337–26344 (2012).

43. Q.-F. Yang, X. Yi, K. Y. Yang, and K. J. Vahala, "Spatial-mode-interaction-induced dispersive waves and their active tuning in microresonators," Optica **3**, 1132–1135 (2016).

44. Y. A. Demchenko and M. L. Gorodetsky, "Analytical estimates of eigenfrequencies, dispersion, and field distribution in whispering gallery resonators," J. Opt. Soc. Am. B **30**, 3056–3063 (2013).

45. I. Breunig, B. Sturman, F. Sedlmeir, H. G. L. Schwefel, and K. Buse, "Whispering gallery modes at the rim of an axisymmetric optical resonator: analytical versus numerical description and comparison with experiment," Opt. Express **21**, 30683–30692 (2013).

46. L. Chang, W. Xie, H. Shu, Q.-F. Yang, B. Shen, A. Boes, J. D. Peters, W. Jin, C. Xiang, S. Liu, G. Moille, S.-P. Yu, X. Wang, K. Srinivasan, S. B. Papp, K. Vahala, and J. E. Bowers, "Ultra-efficient frequency comb generation in AlGaAs-on-insulator microresonators," Nat. Commun. **11**, 1331 (2020).

47. G. Lin and Y. K. Chembo, "Phase-locking transition in Raman combs generated with whispering gallery mode resonators," Opt. Lett. **41**, 3718–3721 (2016).

48. G. Lin, Y. Candela, O. Tillement, Z. Cai, V. Lefèvre-Seguin, and J. Hare, "Thermal bistability-based method for real-time optimization of ultralow-threshold whispering gallery mode microlasers," Opt. Lett. **37**, 5193–5195 (2012).

49. C. Bao, Y. Xuan, C. Wang, A. Fülöp, D. E. Leaird, V. Torres-Company, M. Qi, and A. M. Weiner, "Observation of breathing dark pulses in normal dispersion optical microresonators," Phys. Rev. Lett. **121**, 257401 (2018).

50. A. A. Savchenkov, A. B. Matsko, W. Liang, V. S. Ilchenko, D. Seidel, and L. Maleki, "Kerr frequency comb generation in overmoded resonators," Opt. Express **20**, 27290–27298 (2012).

51. X. Ji, F. A. Barbosa, S. P. Roberts, A. Dutt, J. Cardenas, Y. Okawachi, A. Bryant, A. L. Gaeta, and M. Lipson, "Ultra-low-loss on-chip resonators with sub-milliwatt parametric oscillation threshold," Optica **4**, 619–624 (2017).

52. H. Weng, J. Liu, A. A. Afridi, J. Li, J. Dai, X. Ma, Y. Zhang, Q. Lu, J. F. Donegan, and W. Guo, "Octave-spanning Kerr frequency comb generation with stimulated Raman scattering in an AlN microresonator," Opt. Lett. **46**, 540–543 (2021).

53. B. Hausmann, I. Bulu, V. Venkataraman, P. Deotare, and M. Lončar, "Diamond nonlinear photonics," Nat. Photonics **8**, 369–374 (2014).

54. C. Wang, Z. Fang, A. Yi, B. Yang, Z. Wang, L. Zhou, C. Shen, Y. Zhu, Y. Zhou, R. Bao, Z. Li, Y. Chen, K. Huang, J. Zhang, Y. Cheng, and X. Ou, "High-Q microresonators on 4H-silicon-carbide-on-insulator platform for nonlinear photonics," Light Sci. Appl. **10**, 139 (2021).

55. D. J. Wilson, K. Schneider, S. Hönl, M. Anderson, Y. Baumgartner, L. Czornomaz, T. J. Kippenberg, and P. Seidler, "Integrated gallium phosphide nonlinear photonics," Nat. Photonics **14**, 57–62 (2020).

56. M. Pu, L. Ottaviano, E. Semenova, and K. Yvind, "Efficient frequency comb generation in AlGaAs-on-insulator," Optica **3**, 823–826 (2016).

57. A. G. Griffith, R. K. W. Lau, J. Cardenas, Y. Okawachi, A. Mohanty, R. Fain, Y. H. D. Lee, M. Yu, C. T. Phare, C. B. Poitras, A. L. Gaeta, and M. Lipson, "Silicon-chip mid-infrared frequency comb generation," Nat. Commun. **6**, 6299 (2015).